

# X-ray tomography of extended objects: a comparison of data acquisition approaches

Ming Du<sup>1</sup>, Rafael Vescovi<sup>2,6</sup>, Kamel Fezzaa<sup>2</sup>, Chris Jacobsen<sup>2,3,4</sup>, Doğa Gürsoy<sup>2,5,\*</sup>

<sup>1</sup>Department of Materials Science and Engineering, Northwestern University, Evanston, Illinois 60208, USA

<sup>2</sup>Advanced Photon Source, Argonne National Laboratory, Argonne, Illinois 60439, USA

<sup>3</sup>Department of Physics and Astronomy, Northwestern University, Evanston, Illinois 60208, USA

<sup>4</sup>Chemistry of Life Processes Institute, Northwestern University, Evanston, Illinois 60208, USA

<sup>5</sup>Department of Electrical Engineering and Computer Science, Northwestern University, Evanston, Illinois 60208, USA

<sup>6</sup>Present address: Department of Neurobiology, University of Chicago, Chicago, Illinois 60637, USA

\*Corresponding author: dgursoy@aps.anl.gov

## Abstract

The penetration power of x-rays allows one to image large objects. For example, centimeter-sized specimens can be imaged with micron-level resolution using synchrotron sources. In this case, however, the limited beam diameter and detector size preclude the acquisition of the full sample in a single take, necessitating strategies for combining data from multiple regions. Object stitching involves the combination of local tomography data from overlapping regions, while projection stitching involves the collection of projections at multiple offset positions from the rotation axis followed by data merging and reconstruction. We compare these two approaches in terms of radiation dose applied to the specimen, and reconstructed image quality. Object stitching involves an easier data alignment problem, and immediate viewing of subregions before the entire dataset has been acquired. Projection stitching is more dose-efficient, and avoids certain artifacts of local tomography; however, it also involves a more difficult data assembly and alignment procedure, in that it is more sensitive to accumulative registration error.

## 1 Introduction

X-ray tomography offers a way to image the interior of extended objects, and tomography at synchrotron light sources offers significantly higher throughput than with laboratory sources when working at  $\sim 1$  micrometer voxel resolution or below. However, practical limitations of synchrotron x-ray beam width limit the size of objects that can be studied in single fields of view, and pixel count in readily available image detectors sets a similar limit. Thus it becomes challenging to scale x-ray tomography up from the roughly  $(2000)^3 = 8$  gigavoxel volumes that are routinely imaged today, towards the teravoxel volumes that are required for imaging centimeter-sized objects at micrometer-scale voxel size.

One solution lies in the use of one of several image stitching approaches that can be applied to synchrotron x-ray tomography [1]. Of those approaches discussed, we consider here two of the most promising as shown schematically in Fig. 1:

1. The acquisition of local [2] tomography data (also called truncated object tomography [3], or interior tomography [4]) from an array of positions in the object volume (method III of [1]). In this case the rotation axis is shifted to be centered at each of the array of object positions, after which the object is rotated. The local tomograms of the regions of interest (ROIs) are then reconstructed, and the full object is constructed from stitching together these local tomograms [5]. We refer to this as “object stitching (OS).”
2. The acquisition of “ring in a cylinder” projections where the object is moved to a series of offset positions from the rotation axis, and at each position the object is rotated while projections are collected (method

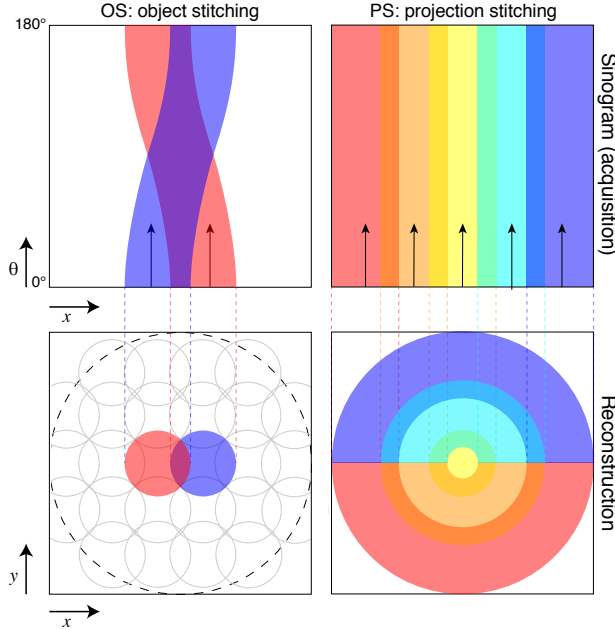


Figure 1: Comparison on the acquisition scheme of object stitching (OS; left) versus projection stitching (PS; right). The top row depicts information collection in sinogram space, where each stripe with an arrow and a distinct color represents one angular scan over  $180^\circ$  (which is then used to synthesize the full  $360^\circ$  sinogram). The bottom row shows the mapping of different scans to the full image. For samples with roughly equal extension in both lateral dimensions, if the number of scans required in PS is  $n_f$ , then  $n_f^2$  scans are needed by OS.

V of [1]). The projections can be assembled and stitched to yield a full-field, panoramic projection image at each rotation angle, or they can be assembled and stitched in the sinogram representation. We refer here to this tomosaic approach [6] as “projection stitching (PS).”

Another approach that has been employed with much success involves collecting a mosaic array of projection images at each rotation angle [7, 8] before repeating the process at the next rotation. For each angle, the projections are assembled and stitched to yield a full-field panoramic projection. However, since in practice it is usually quicker to rotate the specimen through  $180^\circ$  than it is to translate to a new mosaic offset position, this approach (method I of [1]) has lower throughput so we do not consider it further. Other large-scale imaging methods like Helical CT [9] are not discussed here either due to their limitations for high-resolution imaging. Therefore, we limit our discussion to object versus projection stitching as defined above.

Object stitching and projection stitching are two distinct data collection strategies, each with their own tradeoffs. For example, in object stitching one can begin to reconstruct regions of the object immediately after collection of its local tomography data whereas in projection stitching one must wait for the collection of all “ring in a cylinder” data before obtaining a full volume reconstruction. On the other hand, studies in [10] indicates that more care should be taken when reconstructing images from OS data as the method contains inherent complicating factors that can affect image quality. Beyond that, however, we are not aware of systematic studies that compare the characteristics of these two approaches with regards to radiation dose efficiency, a key factor in x-ray microtomography, in addition to reconstruction quality. Low radiation dose is critical for imaging soft materials since they are vulnerable to beam-induced damages and distortions. Moreover, other factors may also come into play when one does either PS or OS in practice. For example, mechanical instabilities in translational motors introduce positional fluctuations of the collected field-of-views, which requires image registration to refine the relative offsets between them. For that, PS and OS data behave differently in the presence of noise. Thus, a comprehensive comparison is made here.

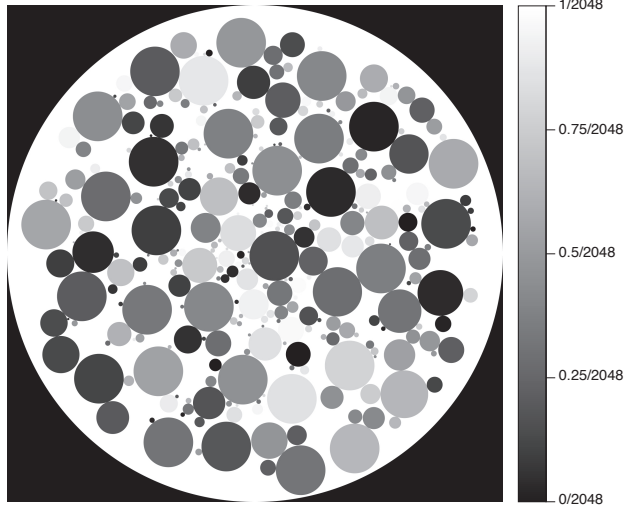


Figure 2: Phantom object created for simulations, where the highest attenuation values are white and the lowest are black. The object has a diameter, or maximum projected thickness, of  $L = 2048$  voxels, each set to a per-voxel linear attenuation coefficient of  $\mu = 1/2048$  so that the total attenuation through the disk if solid is  $\exp[-1]$ . In fact, the object is designed with random spherical “pores” inside with linear attenuation coefficients ranging from  $\mu = 0/2048$  to  $\mu = 1/2048$ .

## 2 Methodology

### 2.1 Phantom object

In order to better understand the tradeoffs between object and projection stitching, we created a 2D phantom sample using the open-source virtual object designing tool *XDesign* [11]. This represents an object slice from a 3D object. The simulated sample (Fig. 2) is a solid disk with a diameter, and thus maximum projected thickness, of  $L = 2048$  pixels. If solid, each pixel would be set to a linear absorption coefficient (LAC) of  $\mu = 1/2048$ , so that its total thickness of  $L = 2048$  pixels would attenuate the x-ray beam by a factor of  $\exp[-\mu L] = \exp[-1]$ . In fact, the object was created with circular pores in its interior, with diameters ranging from 8 to 205 pixels, and linear absorption coefficients ranging from  $\mu = 0/2048$  (vacuum) to  $\mu = 1/2048$  (solid). All pores are randomly distributed with no overlapping. The object is also assumed to be fully within the depth of focus of the imaging system, with no wave propagation effects visible at the limit of spatial resolution, so that pure projection images are obtained. To generate the sinogram of the object, Radon transform was performed using *TomoPy*, an open-source toolkit for x-ray tomography [12]. All tomographic reconstructions in this work are also conducted using this software package.

### 2.2 Sampling for OS and PS

To image an object larger than the imaging system’s field of view  $f$ , one provides some overlap between acquired projection scans. The acquisition scheme can be conveniently shown in the sinogram domain which contains both a spatial dimension and a viewing angle dimension. A scan can be represented by a band-shaped coverage on the sinogram, which is the region where we have access to the measurement. Fig. 3 illustrates such coverage for PS and OS respectively with the same field-of-view size for both schemes. For OS, a  $3 \times 3$  square grid is used. Higher values in the images means that a pixel in the sinogram is sampled for more times.

For OS, by defining a coordination system with the origin  $(0,0)$  located at the object center, it can be shown that the coverage of a local tomography scan centered at  $(x,y)$  is a set of points on the  $360^\circ$  synthesized sinogram given by

$$C_{OS} = \{(s, \theta) | s_0(\theta) - f/2 \leq s \leq s_0(\theta) + f/2\} \quad (1)$$

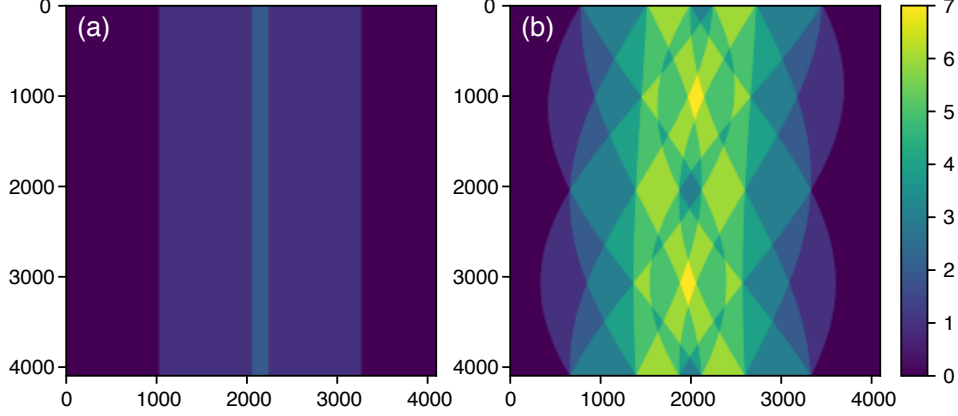


Figure 3: Coverage on the full sinogram in an experiment of (a) PS and (b) OS with equal field-of-view. Values in the images indicate the number of times that a sinogram pixel is sampled.

with

$$s_0(\theta) = \sqrt{x^2 + y^2} \cos(\alpha - \theta) + c_0 \quad (2)$$

where  $s$  and  $\theta$  are respectively the horizontal (spatial) and vertical (angular) coordinates of the sinogram,  $\alpha = \arctan(x/y)$ , and  $c_0$  is the rotation center of the synthesized  $360^\circ$  sinogram. This represents a partial sinogram of the entire object, as shown in Fig. 1. For PS, the coverage is simply a straight band extending through the angular axis. Mathematically, it can be expressed as

$$C_{\text{PS}} = \{(s, \theta) | p - f/2 \leq s \leq p + f/2\} \quad (3)$$

where  $p$  is the center position of the field-of-view.

For object stitching (OS), the partial sinograms are padded with its edge values for twice its width on both sides in order to reduce boundary artifacts in the reconstruction images [10]. After reconstructing all partial sinograms, the reconstructed disks are then stitched together to form the complete reconstruction.

Since both PS and OS involve multiple scans, we define a quantity  $n_f$  that represents the number of scans along one side of the object that is required to fully reconstruct one slice of the sample. For PS,  $n_{f,\text{PS}}$  is equal to the total number of scans; for OS, the total number of scans is roughly  $n_{f,\text{OS}}^2$  considering a square grid of regions of interest (ROIs), though the actual number can vary depending on the object shape. For example, applying OS on a thin sheet-like sample only requires roughly the same number of scans as PS. Also, one could choose hexagonal grids which are more efficient by a factor of  $\sqrt{3}$  than a square grid, but we assume square grids here for simplicity [13].

In order to fully reconstruct one slice of the object using PS, there should be a sufficient number  $n_{f,\text{PS}}$  of scan fields to guarantee that the composite field of view completely covers the longest lateral projection of that slice. In practice, an overlap that takes a fraction  $\gamma_{\text{PS}}$  of the field of view between each pair of adjacent scans is needed for an automated algorithm to determine the offset between them. With this taken into account,  $n_{f,\text{PS}}$  can be denoted as

$$n_{f,\text{PS}} = \text{ceil} \left[ \frac{L - f}{\gamma_{\text{PS}} f} + 1 \right] \quad (4)$$

where the function  $\text{ceil}(x)$  is the ceiling function that returns the smallest integer that is greater than or equal to a real number  $x$ . Since the overlapping area diminishes the actual sample area that a scan can cover, we introduce a “useful field of view”  $f'_{\text{PS}}$  for PS, given by  $f'_{\text{PS}} = \gamma_{\text{PS}} f$ . For example, if a 15% overlap is deliberately created between a pair of adjacent scans, then  $f'_{\text{PS}}$  will be 85% of the instrumental field-of-view. Unless otherwise noted, in this work we keep the value of  $\gamma_{\text{PS}}$  to be 0.85 for simulation studies.

The case for OS differs in that the scans needs to cover the object slice in two dimensions. In principle, the scans in OS can be arranged in an arbitrary pattern that complies with the actual shape of the sample. If the sample is square, then a roughly equal number of scans  $n_{f,\text{OS}}$  is needed along both sides of the object,



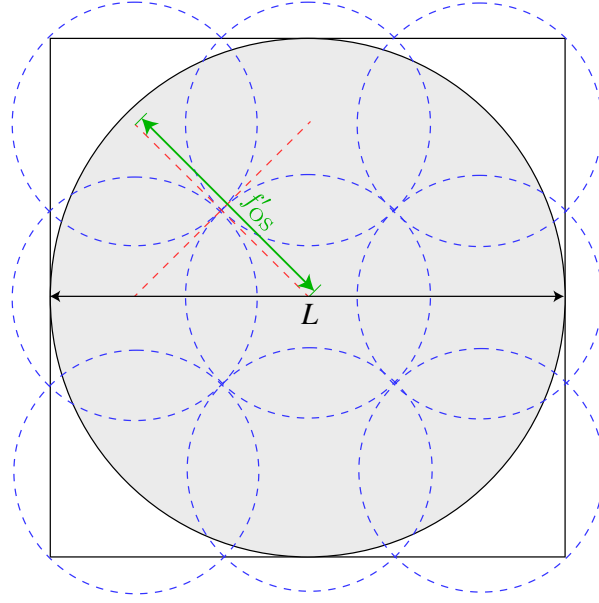


Figure 4: Schematic diagram showing the assumed pattern of data acquisition in the OS approach of beyond-field-of-view tomography. The specimen is represented by the gray solid disk. Each local ROI that can be reconstructed using the data acquired from a scan in OS is shown by a dashed blue circle. Each of these ROIs has a diameter of  $f'_{OS}$ , and they are packed in a way that the distance between the centers of each pair of diagonally adjacent ROIs is exactly  $f'_{OS}$ , so that the sample can be fully covered without gaps.

or  $n_{f,OS}^2$  scans in total. A special notice should be paid to the width of the field of view in OS, as it might not be equal to the actual field of view of the optical system. In OS, it has been found that the reconstructed ROI often exhibits a bowl-shaped intensity profile, with values of near-boundary pixels abnormally higher [10]. Although this can be mitigated by padding the partial sinograms, this remedy does not work effectively when the truncation ratio is very low. In such scenario, the reconstructed ROIs need to have a portion of their outer pixels removed before they can be stitched. Similar to the case of PS, we therefore introduce a “useful field of view”  $f'_{OS}$  for OS. If we use for object stitching only the content within a disk whose radius is a fraction  $\gamma_{OS}$  of the original ROI, then  $f'_{OS} = \gamma_{OS}f$ . Consequently, the required number of scans  $n_{f,OS}$  is given by

$$n_{f,OS} = \begin{cases} 1 & f \geq L \\ \text{ceil}\left(\frac{\sqrt{2}L}{\gamma_{OS}f}\right) & f < L \end{cases} \quad (5)$$

We emphasize that  $n_{f,OS}$  is the number of scans required along one side of the sample; for a square specimen, the total number of scans needed is  $n_{f,OS}^2$ . Eq. 5 is derived assuming the scenario indicated in Fig. 4. When  $f < L$ , scanned ROIs are arranged in a square grid such that each corner of the bounding square of the sample disk intersects with the border of an ROI. Also, we assume that the distance between the centers of two diagonally overlapping ROIs is  $f'_{OS}$  so that all ROIs exactly cover the object seamlessly. Unless specifically indicated, the value of  $\gamma_{OS}$  is chosen to be 0.85 for simulation studies involved in this work.

In order to understand the consequences of different object diameters  $L$ , we follow previous work [10] and characterize these consequences in terms of a truncation ratio  $T$  of

$$T = \frac{f'}{L} \quad (6)$$

where of course one uses  $f'_{OS}$  for object stitching (OS) and  $f'_{PS}$  for projection stitching (PS).

### 2.3 Radiation dose calculation

The differential energy deposition  $dE$  within an infinitesimal depth  $dt$  is formulated from the Lambert-Beer law as

$$\frac{dE}{dt} = \left| \bar{n} E_0 \frac{dI}{dt} \right| \quad (7)$$

where  $\bar{n}$  is the average number of incident photons per voxel, and  $E_0$  is the photon energy. The Lambert-Beer law gives  $\mu_{\mathbf{r}}(t)$ , the x-ray LAC of the sample as a function of penetration depth  $t$  along the current transmission direction  $\mathbf{r}$ , as  $\mu_{\mathbf{r}}(t) = -[1/I(t)](dI/dt)$ . To simplify our later computation with this term included in an integral with regards to  $t$ , we approximate the quantity  $I(t)$  in the factor prior to  $dI/dt$  as  $I(t) \approx I(L/2) = \exp(-\bar{\mu}L/2)$ , where  $\bar{\mu}$  is the mean LAC of the specimen. Equation 7 then becomes

$$\frac{dE}{dt} = \bar{n} E_0 \exp(-\bar{\mu}L/2) \mu_{\mathbf{r}}(t). \quad (8)$$

Again, the term  $\exp(-\bar{\mu}L/2)$  represents the beam attenuation factor at the center of the object, but it can also be used to approximate the average normalized beam intensity “seen” by an arbitrary voxel of the object in one viewing direction. Accordingly, we also replace  $\mu_{\mathbf{r}}(t)$  in Eq. 9 with a constant value of  $\bar{\mu}$ . This approximation is valid as long as the LAC of the object varies slowly. By integrating both sides over the voxel size  $\Delta$ , we obtain the energy absorbed by this voxel as

$$E = \bar{n} E_0 \exp(-\bar{\mu}L/2) \bar{\mu} \Delta. \quad (9)$$

Then, the radiation dose received by this  $j$ -th voxel per  $(180^\circ)$  scan is given by

$$D_{s,j} = \frac{N_\theta \bar{n} E_0 \exp(-\bar{\mu}L/2) \bar{\mu}}{\rho \Delta^2} \quad (10)$$

where  $N_\theta$  is the number of projection angles, and  $\rho$  is the object density. The subscript  $s$  in  $D_{s,j}$  denotes the  $s$ -th scan. Again, for PS, a total of  $n_{f,PS}$  scans are needed, while for OS the number is on the order of  $n_{f,OS}^2$ . Based on this, one can estimate the total radiation dose received by the sample by summing up the number of occasions of being exposed to the beam over all voxels ( $j$ ) and all scans ( $s$ ). This is compactly expressed as

$$\begin{aligned} D &= \sum_s \sum_j D_{s,j} \\ &\propto \sum_s \epsilon \Omega_s \end{aligned} \quad (11)$$

where  $\Omega_s$  is the total area in sinogram domain that is sampled in one scan (which is equal to the width in pixels of a field of view multiplied by the number of projection angles), and  $\epsilon$  is the fraction of pixels where the sample is present (*i.e.*, pixels that are not purely air).

### 2.4 Experimental data acquisition and registration

For an experimental tests on projection stitching (PS), we used experimental data collected using 25 keV X rays at beamline 32-ID of the Advanced Photon Source. The specimen is a truncated charcoal sample with a diameter of  $d = 4$  mm, whereas the imaging system field of view was  $f = 1920 \times 0.6 \mu\text{m} = 1.12$  mm. With  $\gamma_{PS} = 0.9$ , this yields a reduced field of view of  $f'_{PS} = 1.04$  mm so that  $n_{f,PS} = 4$  and  $T = 0.26$ . Registration of the sinograms was done using phase correlation, which can be formulated as

$$\mathbf{c} = \underset{\mathbf{x} \in \mathbb{R}^2}{\operatorname{argmax}} \mathcal{F}^{-1} \left[ \frac{\mathcal{F}[I_a(\mathbf{x})] \mathcal{F}[I_b^*(\mathbf{x})]}{|\mathcal{F}[I_a(\mathbf{x})] \mathcal{F}[I_b^*(\mathbf{x})]|} \right] (\mathbf{x}). \quad (12)$$

This method is reliable when a large number of high-contrast features are present in the overlapping region of both images  $I_a$  and  $I_b$ , and when noises are not heavily present. In practice, photon flux ( $\bar{n}$  in Eq. 10) sometimes needs to be reduced in order to lower the radiation dose imposed on the sample. This can lead to higher photon noise that challenges image registration.

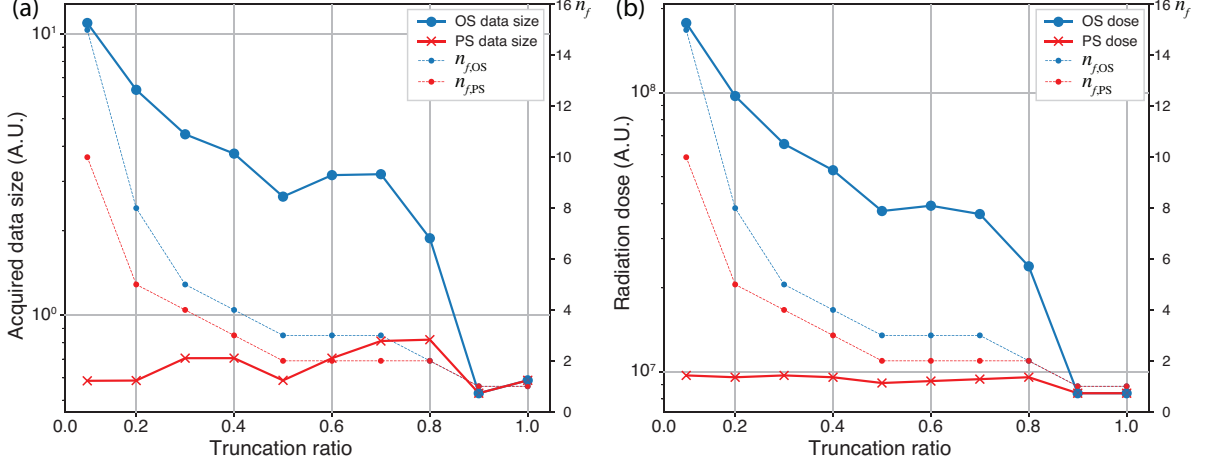


Figure 5: Acquired data size (a) and radiation dose (b) as a function of the truncation ratio  $T$  of Eq. 6 for both object stitching (OS) and projection stitching (PS). In each subplot, the variation of  $n_{f,PS}$  and  $n_{f,OS}$  is also shown. The figure indicates that the acquired data size and radiation dose do not necessarily decrease with increasing truncation ratio; rather, both quantities are associated with the arrangement of scans in an actual experiment. These results were calculated for fixed values of  $\gamma_{PS} = 0.85$  and  $\gamma_{OS} = 0.85$  as discussed in the text.

### 3 Results and discussion

#### 3.1 Comparison on dose-efficiency

As one can easily see from Fig. 1, object stitching (OS) requires a larger number of scans than projection stitching (PS) by a factor of about  $1/T$ . Because much of the illumination of one scan goes into out-of-local-tomogram regions in object stitching, this also means that the object is exposed to a higher radiation dose. In Eq. 11, the total radiation dose of an experiment is shown to be approximately proportional to the area of non-air regions sampled in the sinogram, given that the sample does not contain large fluctuations in absorption coefficient. In this equation,  $\Omega_s$  itself is also an interesting quantity to investigate. The sum of the areas of all  $\Omega_s$  regions in the sinogram, which also includes those “air” pixels, provides an intuitive measurement of the acquired data size, which is jointly determined by the actual field of view, the number of scans  $s$ , and the number of projection angles  $N_\theta$ . For a given experimental configuration, this summed area is denoted by  $A$ . A lower  $A$  means that the sample can be entirely imaged and reconstructed with a smaller data size, which is desirable in the case where only limited storage and computing resources are available.

With these quantities defined, Fig. 5(a) shows the results for acquired data size  $A_{PS}$  and  $A_{OS}$  as a function of truncation ratio  $T$ , while Fig. 5(b) shows  $D_{PS}$  and  $D_{OS}$ . The dashed lines in each plot show the variation of  $n_{f,PS}$  and  $n_{f,OS}$ . Note that  $n_{f,OS}$  is the number of scans along one side of the object, so that  $n_{f,OS}^2$  scans are required for object stitching (OS). When examining this figure, it has to be noted that no matter what  $T$  is, the values of  $\gamma_{PS}$  and  $\gamma_{OS}$  are fixed. This means that area covered by all scans in either PS or OS might be larger than the sample. In such cases, we allow acquisition to extend beyond the right side of the sample for PS; for OS, the exceeded margins are on the right and bottom sides of the sample. The “overflow” of acquisition does not substantially affect  $D$ , but can increase  $A$ . It can be seen in Fig. 5(a) that  $A$  is not a monotonic function of  $T$ , although it does show an overall decreasing trend with increasing  $T$ . For example, when  $T$  grows from 0.5 to 0.7,  $A_{OS}$  increases while  $n_{f,OS}$  is unchanged. This is explained by the larger “overflow” of scanned field beyond the actual object. In contrast, the increase in  $T$  that does not cause a reduction of  $n_f$  only results in a small cost of  $D$  due to the increase of overlapping areas required between adjacent scans. However, the overall observation is still that PS is both more data-efficient and dose-efficient than OS in general. However the figures indicate that no matter which method is used, a higher  $T$  does not necessarily imply a better data efficiency in the case of  $f < L$ . One should thus carefully choose the camera to use in order to optimize the experiment in terms of both data size and radiation dose.

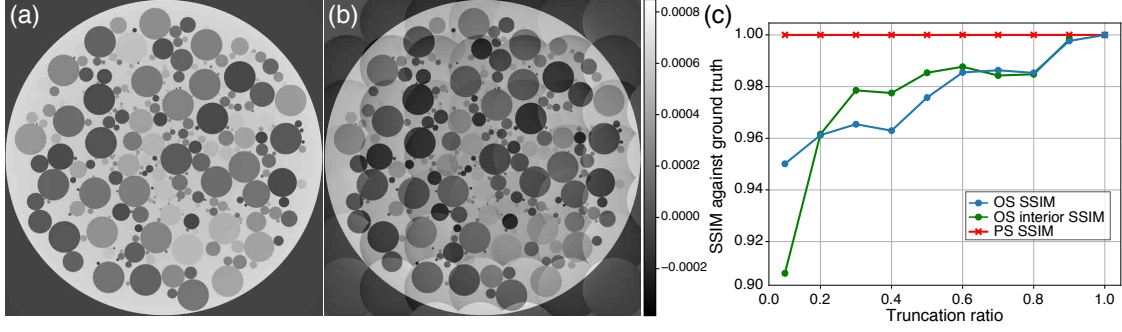


Figure 6: Comparison of image quality between object stitching (OS) and projection stitching (PS). This comparison is made using the Structural SIMilarity (SSIM) with regards to the ground truth image (a), against reconstructions for PS (not shown) and OS (b). Also shown (c) is the SSIM as a function of truncation ratio  $T$ .

### 3.2 Comparison on reconstruction artifacts

While both OS and PS are subject to photon noises during measurement, other types of artifacts can also participate in determining the reconstruction quality. The sources of noise and artifacts in the final reconstructions for PS are straightforward to understand. In particular, when the intensity of adjacent projection tiles differs, ring artifacts can be seen in the reconstruction if the sinograms are not properly blended where they overlap. For OS, reconstruction quality is mainly affected by three factors other than noise in the raw data. First, since the illuminating beam at different scan positions and illumination angles arrive at the object region with varying transmission through out-of-object-field features, the overall intensity of the reconstruction disk can vary between neighboring tiles. Second, a bowl-shaped intensity profile across an individual reconstruction disk is often observed in ROI tomography, in which case the pixel intensities near the edge of the reconstruction disk are shifted higher. This can be alleviated by padding the partial sinograms on its left and right sides (along the spatial axis) by the edge values [10]. In our case, the sinograms were padded by twice of their length on each side, but this did not completely eliminate distortion in the intensity profile. Finally, each projection image collected inevitably contains information of the portion object lying outside of the ROI, which, at least to some minor extent, violates the Fourier slice theorem [14]. Ideally, one would also seek to satisfy the Crowther criterion [15] on the required number of rotation angles based on the entire object size rather than the size of the local tomography region of interest. One can thus expect aliasing artifacts especially for low truncation ratios.

To quantify the reconstruction quality, we used Structural SIMilarity (SSIM; [16]) as a metric for the fidelity of the stitched reconstruction images with regards to the ground truth image. The reconstruction images were obtained by applying filtered backprojection (FBP) algorithm to the full-object sinogram. SSIM is defined as a product of three terms that assess the similarity between two images  $A$  and  $B$  in different aspects. These include the luminance ( $l$ ), the contrast ( $c$ ), and the structure ( $s$ ), defined by

$$l(A, B) = \frac{2\mu_A\mu_B + c_1}{\mu_A^2 + \mu_B^2 + c_1} \quad (13)$$

$$c(A, B) = \frac{2\sigma_A\sigma_B + c_2}{\sigma_A^2 + \sigma_B^2 + c_2} \quad (14)$$

$$s(A, B) = \frac{\sigma_{AB} + c_3}{\sigma_A\sigma_B + c_3} \quad (15)$$

where

$$c_1 = (k_1 L)^2 \quad (16)$$

$$c_2 = (k_2 L)^2 \quad (17)$$

$$c_3 = c_2/2 \quad (18)$$

with typical values of  $k_1$  and  $k_2$  set to 0.01 and 0.03, and  $L$  being the dynamic range of the grayscale images. In Eqs. 13 to 15,  $\mu_i$  and  $\sigma_i$  represent the mean and standard deviation of image  $i$  ( $i = A$  or  $B$ ), and  $\sigma_{AB}$  is the covariance of image  $A$  and  $B$  [16]. While it is common to calculate the SSIM as the product of all three terms, we set  $l(A, B) = 1$  here in order to exclude the overall intensity shifting and scaling. Thus for all quality evaluations in this work, we have

$$\text{SSIM}(A, B) = c(A, B) \cdot s(A, B). \quad (19)$$

Figs. 6(a) and (b) respectively show the stitched reconstructions obtained from PS and OS with  $T = 0.2$ . If the beam brightness is sufficiently high and stable, then noise and intensity variations between adjacent tiles can be neglected. In this case, the stitched sinogram in PS is not affected by other systematic artifacts, and is identical to the full-object sinogram. However, the stitched reconstruction in OS is affected by intensity variations and bowl-profile artifacts, even though the partial sinograms were padded before reconstruction and only the inner  $\gamma_{\text{OS}} = 0.85$  of the reconstructed ROIs were used. Fig. 6 plots the SSIM of the reconstructed porous disk (vacuum portions at the corners are not included) with regards to the ground truth for both two approaches. As can be seen, the quality of the PS reconstruction is in principle not affected by the truncation ratio. In contrast, an overall reduction in SSIM with decreasing truncation ratio is seen for OS. In order to examine how the truncation ratio  $T$  influences the reconstruction quality of an individual reconstruction disk in OS, we also computed the mean SSIM of the inner portions in all reconstructed ROIs that are far from the boundaries and termed it the “OS interior SSIM” in Fig. 6. In this way, the influence of the bowl-profile artifacts can be excluded. As in Fig. 6, this SSIM also drops with diminishing  $T$ . This indicates that in addition to boundary artifacts, a low truncation ratio also deteriorates the intrinsic reconstruction quality of the ROI, which is mainly in the form of noise caused by out-of-ROI information.

### 3.3 Comparison on image registration feasibility

Registration refers to the processing of finding the relative positional offset between adjacent tiles in mosaic tomography. For PS, registration is done in projection domain before merging the partial datasets. OS, on the other hand, involves registration on reconstructed images. The large number of tiles in mosaic tomography poses huge difficulties for manual registration, and automatic registration methods are usually employed. Phase correlation (PC) is the most popular registration algorithm, where the offset vector  $\vec{c}$  between two images  $I_a$  and  $I_b$  is determined by

$$\vec{c} = \text{argmax} \left( \mathcal{F}^{-1} \left[ \frac{\mathcal{F}[I_a(\vec{x})]\mathcal{F}[I_b^*(\vec{x})]}{|\mathcal{F}[I_a(\vec{x})]\mathcal{F}[I_b^*(\vec{x})]|} \right] (\vec{x}) \right). \quad (20)$$

In Eq. 20,  $\mathcal{F}$  is the Fourier transform operator, and  $I_i^*$  represents the complex conjugate of  $I_i$ .

The transmission radiographs for specimens that are thick and not entirely periodic generally do not exhibit a good number of distinguishable fine features, because the microstructures of the materials tend to entangle and blend into each other when they are superposed along the beam path. However, this does not imply that PS projections are intrinsically harder objects for registration compared to OS reconstructions. Although it is conceptually plausible that more high-frequency features arise in reconstructed images, we should notice that phase correlation is a technique that is susceptible to noise. When data are collected with low photon flux, Poisson noise is more pronounced, and tomographic reconstructions based on the Fourier slice theorem can be more heavily affected by noises due to the amplification of high-frequency artifacts induced by the ramp filter [14], though this issue might be mitigated by adding another low-pass filter. To demonstrate this, a numerical study is presented below. To simulate registration in PS, we created a projection panorama of our whole charcoal specimen, and extract a row of  $1024 \times 1024$  tiles from it with a constant interval of 850 pixels. As the projection panorama was normalized using the dark field and white field data, all tiles extracted contain pixels with values ranging between 0 and 1. Here we denote the image by  $I$ . We then define a scaling factor  $n_{\text{ph}}$  to represent a “mean” photon count for each pixel. In other words,  $n_{\text{ph}}$  is the number of photons incident on a pixel of the acquired radiograph. Poisson noises was subsequently applied to all tiles, using the probably density function of

$$f(k, n_{\text{ph}}I) = \frac{(n_{\text{ph}}I)^k e^{-n_{\text{ph}}I}}{k!} \quad (21)$$

where  $k$  is the actual number of photon count. The noisy version of the tiles were then enhanced by taking their negative logarithm, and registered using phase correlation. For OS, different levels of Poisson noise were added to extracted partial sinograms, from which reconstruction images were subsequently created and registered. The field of view in this case is 1024 pixels. Since data fidelity is guaranteed only within a disk for an OS reconstruction, we use a smaller offset of 700 pixels in both the  $x$  and  $y$  directions in order to compensate the smaller usable overlapping area. Figure 7(a) compares the registration accuracy of OS and PS over a range of photon budgets per pixel, which is the total number of photons to be applied to a specimen voxel during the experiment. Thus, all comparisons between OS and PS are based on the condition that the total radiation doses are equal. The photon budget is evenly distributed to all scans and  $n_{\text{ph}}$  is calculated accordingly, in which case OS will have a lower  $n_{\text{ph}}$  in a single scan compared to PS. For our test data, the mean registration error of PS is always below 1, while OS requires a photon budget of about 2000 for the mean error to diminish into the sub-pixel level.

The number of projection angles can also impact the registration accuracy for OS since it is done in the reconstruction domain. In Fig. 7(b), the mean registration error is plotted with regards to the level of downsampling in the axis of projection angles. The original data involves 4500 projections, which is downsampled by factors of powers of 2. The result indicates that the error starts to exceed the pixel-level boundary when the downsampling level is larger 4.

A critical drawback of PS is that registration errors are accumulative, which means that deviations in the offset determined for any pair of tiles can affect the quality of a large part or even the entirety of the final reconstruction. On the other hand, registration errors in OS involve multiple tiles intersecting on several sides, giving less opportunity for alignment pathologies along one edge to dominate global alignment. For PS, the accumulated registration error throughout a row in the tile grid would cause the relative center of rotation to deviate from the true value for tiles that are far away from the rotation axis. Since the reconstruction of PS takes the registration results as an input, this can lead to off-center distortions on small features at some locations of the full reconstruction. To show this, we compare the reconstructions for a part of the data collected from our charcoal sample. To simulate the PS result with induced error, we extracted 8 tiles from the full sinogram with a fixed interval of 795 pixels. The registered positions of all tiles were then deliberately adjusted by errors following a Gaussian distribution with a standard deviation of 4, after which they were stitched and reconstructed. The center of rotation set for the reconstructor was determined to optimize the reconstruction quality of the central region of the sample. The OS results serving as a reference were obtained by extracting partial sinograms from the full sinogram, and then reconstructing them individually. Using these procedures, we show in Fig. 8 a comparison of two local regions of the reconstructions obtained using PS and OS, respectively. One of these regions is exactly at the object center, while the other one is around 1000 pixels above in the object slice view. The positions of both regions are marked on the full reconstruction slice. For the central region (shown in the second row of the image grid in Fig. 8), the exhibited images have nearly the same quality. However, for the off-center region, some dot-shaped features extracted from the PS reconstruction become heavily distorted (as marked by the colored arrows in the PS figure on the first row of the grid). This indicates an erroneous registration outcome for the tile contributing to this region, which deviates the distance of the projections contained in this tile to the rotation center away from the accurate value. When the tiles are correctly registered, as shown in the inset of the PS figure, the distortion no longer exists.

Object stitching (OS) reconstructions are not globally affected by registration errors. We further note that in addition to this feature, OS is advantageous compared to PS in several other aspects. For certain sample geometries, OS can achieve better dose efficiency than PS by using more projection angles for highly interesting regions of the sample while using fewer angles for the rest. Also, OS allows one to flexibly select reconstruction methods or parameters for different ROIs. For example, an ROI where features lie in textured backgrounds can be reconstructed using Bayesian methods with stronger sparsity regularization in order to suppress background structures.

## 4 Conclusion

We have compared two methods for tomography of objects that extend beyond the field of view of the illumination system and camera, based on their radiation dose, reconstruction fidelity, and the presence of

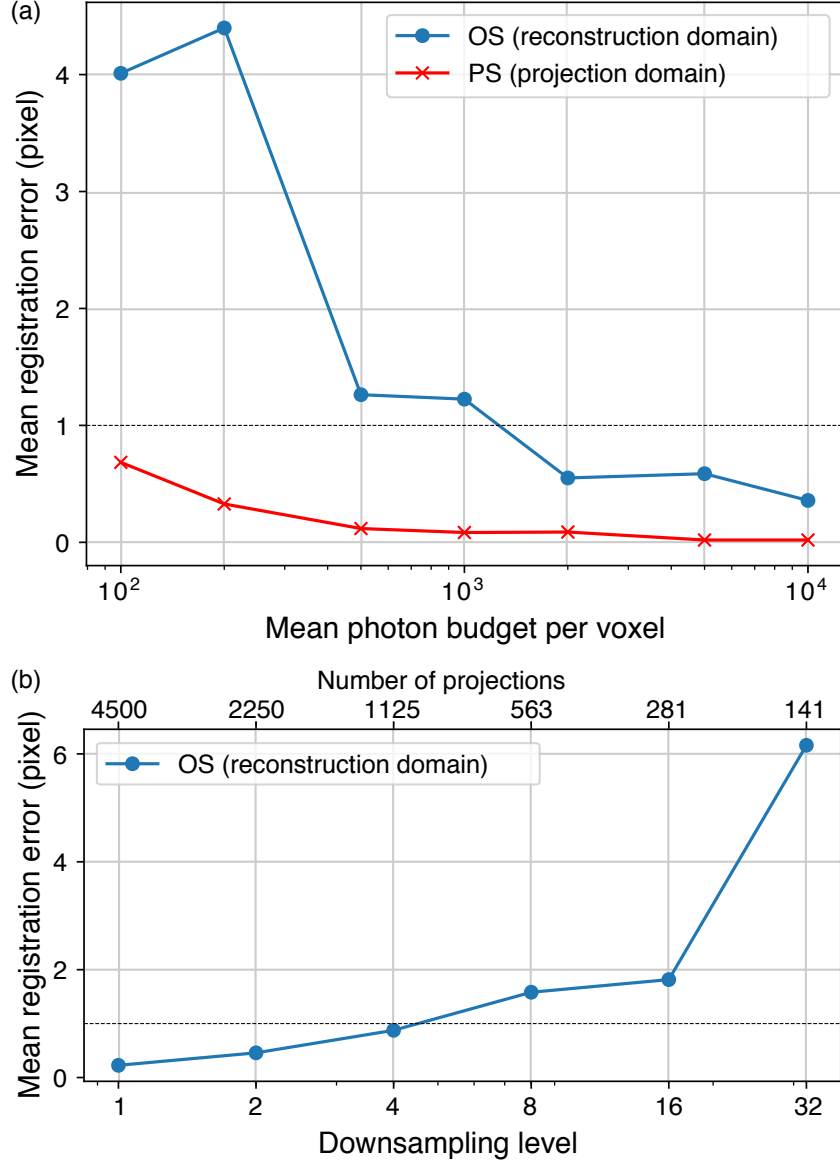


Figure 7: Mean registration error plotted against (a) the average photon budget per voxel for both PS and OS, and (b) the downsampling level in projection angles for OS. The plot indicates that the accuracy of phase correlation degrades when projection images become more noisy due to lower number of incident photons. For this particular sample, registration in reconstruction domain for OS requires a higher incident photon flux in order to give reliable registration results. In addition, a reduction in projection angles also causes a significant deterioration in registration accuracy for OS.

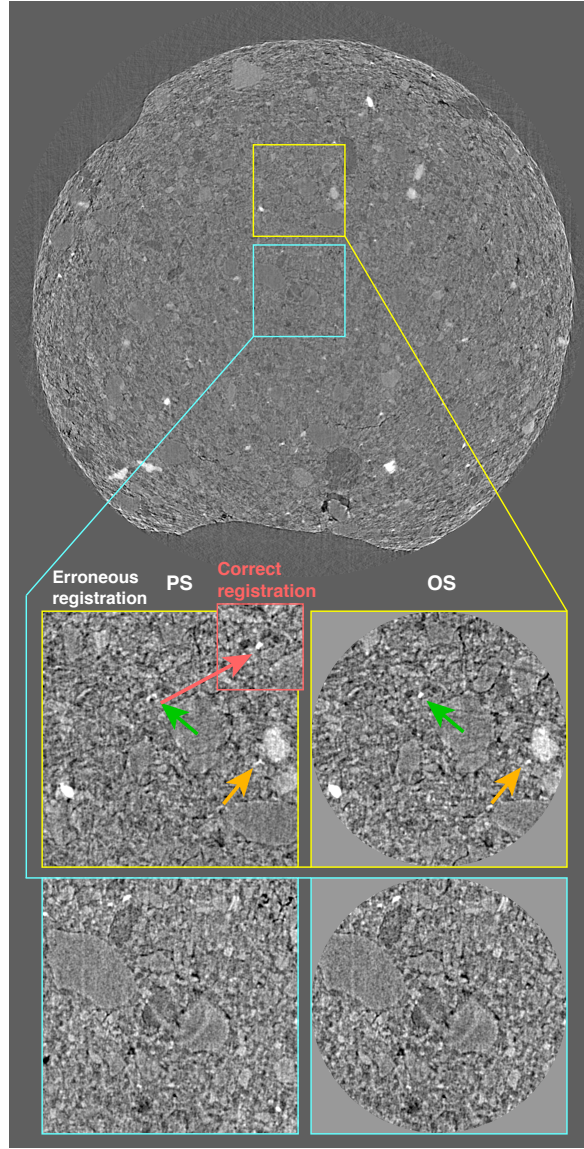


Figure 8: Comparison of the effect of registration errors. Shown here are projection stitching (PS; left column in the grid) and object stitching (OS; right column) reconstructions at an region-of-interest (first row) and the center (second row) of a slice in the charcoal sample. The PS reconstruction was done by stitching 8 tiles extracted from the full sinogram. Registration errors following a Gaussian distribution with a standard deviation of 4.0 were exerted to the tile positions before stitching. The rotation center for PS reconstruction was calibrated to optimize the quality around the object center. As a result, the central region of the charcoal reconstructed using both methods appears similar. However, at around 1000 pixels above the object center, the PS reconstruction shows severe distortion of dot-features (pointed by colored arrows) due to the deviation of its actual position from the rotation center inputted to the reconstruction routine. The inset in the PS figure shows the appearance of one of the distorted features when the tiles are correctly registered.



registration artifacts. Projection stitching (PS) gives lower radiation dose, and it is also generally free of inter-tile intensity variations, in-tile intensity “bowl” artifacts, and noise induced by out-of-local-tomogram information. In addition, tile registration is shown to be no harder than with object stitching (OS), especially when the noise level is high. The major drawback of PS is that registration errors are accumulative and can affect the entire reconstruction. Our present efforts are directed towards providing more reliable registration algorithms in order to improve the reconstruction quality of PS for thick amorphous samples; one approach that offers promise is iterative reprojection [17, 18, 19], though it will be computationally demanding for large datasets.

## 5 Acknowledgement

This research used resources of the Advanced Photon Source and the Argonne Leadership Computing Facility, which are U.S. Department of Energy (DOE) Office of Science User Facilities operated for the DOE Office of Science by Argonne National Laboratory under Contract No. DE-AC02-06CH11357. We thank the National Institute of Mental Health, National Institutes of Health, for support under grant U01 MH109100. We also thank Vincent De Andrade for his help with acquiring the data on the charcoal sample shown in the paper.

## References

- [1] Kyrieleis, A., Ibison, M., Titarenko, V. & Withers, P. J. Image stitching strategies for tomographic imaging of large objects at high resolution at synchrotron sources. *Nuclear Instruments and Methods in Physics Research A* **607**, 677–684 (2009).
- [2] Kuchment, P., Lancaster, K. & Mogilevskaya, L. On local tomography. *Inverse Problems* **11**, 571–589 (1995).
- [3] Lewitt, R. M. & Bates, R. H. T. Image reconstruction from projections: I: General theoretical considerations. *Optik* **50**, 19–33 (1978).
- [4] Natterer, F. *The Mathematics of Computerized Tomography* (John Wiley & Sons, Chichester, 1986).
- [5] Oikonomidis, I. V. & Lovric, G. Imaging samples larger than the field of view: the SLS experience. *Journal of Physics: Conference Series* **849**, 012004 (2017).
- [6] Vescovi, R. F. C., Cardoso, M. B. & Miqueles, E. X. Radiography registration for mosaic tomography. *Journal of Synchrotron Radiation* **24**, 686–694 (2017).
- [7] Liu, Y. *et al.* TXM-Wizard: a program for advanced data collection and evaluation in full-field transmission x-ray microscopy. *Journal of Synchrotron Radiation* **19**, 281–287 (2012).
- [8] Mokso, R. *et al.* X-ray mosaic nanotomography of large microorganisms. *Journal of Structural Biology* **177**, 233–238 (2012).
- [9] Silverman, P. M., Cooper, C. J., Weltman, D. I. & Zeman, R. K. Helical CT: practical considerations and potential pitfalls. *RadioGraphics* **15**, 25–36 (1995).
- [10] Kyrieleis, A., Titarenko, V., Ibison, M., Connolley, T. & Withers, P. J. Region-of-interest tomography using filtered backprojection: assessing the practical limits. *Journal of Microscopy* **241**, 69–82 (2010).
- [11] Ching, D. J. & Gürsoy, D. XDesign: an open-source software package for designing x-ray imaging phantoms and experiments. *Journal of Synchrotron Radiation* **24**, 537–544 (2017).
- [12] Gürsoy, D., De Carlo, F., Xiao, X. & Jacobsen, C. TomoPy: a framework for the analysis of synchrotron tomographic data. *J. Synchrotron Rad* (2014). *21*, 1188–1193 [*doi:10.1107/S1600577514013939*] **21**, 1–6 (2014).
- [13] Heinzer, S. *et al.* Hierarchical microimaging for multiscale analysis of large vascular networks. *NeuroImage* **32**, 626–636 (2006).

- [14] Kak, A. C. & Slaney, M. *Principles of Computerized Tomographic Imaging* (Society for Industrial and Applied Mathematics, 2012).
- [15] Crowther, R. A., DeRosier, D. J. & Klug, A. The reconstruction of a three-dimensional structure from projections and its application to electron microscopy. *Proceedings of the Royal Society of London A* **317**, 319–340 (1970).
- [16] Wang, Z., Bovik, A. C., Sheikh, H. R. & Simoncelli, E. P. Image quality assessment: From error visibility to structural similarity. *IEEE T. Image Process.* **13**, 600–612 (2004).
- [17] Dengler, J. A multi-resolution approach to the 3d reconstruction from an electron microscope tilt series solving the alignment problem without gold particles. *Ultramicroscopy* **30**, 337–348 (1989).
- [18] Latham, S. J., Kingston, A. M., Recur, B., Myers, G. R. & Sheppard, A. P. Multi-resolution radiograph alignment for motion correction in x-ray micro-tomography. *Proceedings SPIE* **9967**, 996710 (2016).
- [19] Gürsoy, D. *et al.* Rapid alignment of nanotomography data using joint iterative reconstruction and reprojection. *Scientific Reports* **7**, 11818 (2017).